

99 Herculis: Host to a Circumbinary Polar-ring Debris Disk

G. M. Kennedy^{*1}, M. C. Wyatt¹, B. Sibthorpe², G. Duchêne^{3,4}, P. Kalas⁴,
B. C. Matthews^{5,6}, J. S. Greaves⁷, K. Y. L. Su⁸, M. P. Fitzgerald^{9,10}

¹ *Institute of Astronomy, University of Cambridge, Madingley Road, Cambridge CB3 0HA, UK*

² *UK Astronomy Technology Center, Royal Observatory, Blackford Hill, Edinburgh EH9 3HJ, UK*

³ *Department of Astronomy, University of California, B-20 Hearst Field Annex, Berkeley, CA 94720-3411, USA*

⁴ *Laboratoire d'Astrophysique, Observatoire de Grenoble, Université J. Fourier, CNRS, France*

⁵ *Herzberg Institute of Astrophysics, National Research Council Canada, 5071 West Saanich Road., Victoria, BC, Canada, V9E 2E7, Canada*

⁶ *University of Victoria, Finnerty Road, Victoria, BC, V8W 3P6, Canada*

⁷ *School of Physics and Astronomy, University of St Andrews, North Haugh, St Andrews, Fife KY16 9SS, UK*

⁸ *Steward Observatory, University of Arizona, 933 North Cherry Avenue, Tucson, AZ 85721, USA*

⁹ *Institute of Geophysics and Planetary Physics, Lawrence Livermore National Laboratory, L-413, 7000 East Avenue, Livermore, CA 94550, USA*

¹⁰ *Department of Physics and Astronomy, UCLA, Los Angeles, CA 90095-1547, USA*

11 January 2012

ABSTRACT

We present resolved *Herschel* images of a circumbinary debris disk in the 99 Herculis system. The primary is a late F-type star. The binary orbit is well characterised and we conclude that the disk is misaligned with the binary plane. Two different models can explain the observed structure. The first model is a ring of polar orbits that move in a plane perpendicular to the binary pericenter direction. We favour this interpretation because it includes the effect of secular perturbations and the disk can survive for Gyr timescales. The second model is a misaligned ring. Because there is an ambiguity in the orientation of the ring, which could be reflected in the sky plane, this ring either has near-polar orbits similar to the first model, or has a 30 degree misalignment. The misaligned ring, interpreted as the result of a recent collision, is shown to be implausible from constraints on the collisional and dynamical evolution. Because disk+star systems with separations similar to 99 Herculis should form coplanar, possible formation scenarios involve either a close stellar encounter or binary exchange in the presence of circumstellar and/or circumbinary disks. Discovery and characterisation of systems like 99 Herculis will help understand processes that result in planetary system misalignment around both single and multiple stars.

Key words: circumstellar matter — stars: individual: 99 Herculis, HD 165908, HIP 88745, GJ704AB

1 INTRODUCTION

The *Herschel* Key Program DEBRIS (Dust Emission via a Bias free Reconnaissance in the Infrared/Submillimeter) has observed a large sample of nearby stars to discover and characterise extrasolar analogues to the Solar System’s asteroid and Kuiper belts, collectively known as “debris disks.” The 3.5m *Herschel* mirror diameter provides 6-7” resolution at 70-100 μ m (Pilbratt et al. 2010), and as a consequence our survey has resolved many disks around stars in the Solar neighbourhood for the first time (Matthews et al. 2010; Churcher et al. 2011).¹

* Email: gkennedy@ast.cam.ac.uk

¹ *Herschel* is an ESA space observatory with science instruments provided by European-led Principal Investigator consortia and with important participation from NASA.

Here we present resolved images of the 99 Herculis circumbinary disk. This system is particularly interesting because unlike most debris disk+binary systems, the binary orbit is well characterised. The combination of a known orbit and resolved disk means we can compare their (different) inclinations and consider circumbinary particle dynamics and formation scenarios.

This system is a first step toward building on the binary debris disk study of Trilling et al. (2007). Their *Spitzer* study found that debris disks are as common in binary systems as in single systems, but tend not to have separations in the 3-30AU range. However, only some of their systems had detections at multiple wavelengths to constrain the disk location and none were resolved, making the true dust location uncertain. Resolved systems such as 99 Her remove this ambiguity, and

Table 1. 99 Her orbital elements, system mass and 1σ uncertainties. The ascending node Ω is measured anti-clockwise from North. The longitude of pericenter is measured anti-clockwise from the ascending node, and projected onto the sky plane has a position angle of 163° (i.e. is slightly different to $41+116$ because the orbit is inclined).

Parameter	Symbol (unit)	Value	Uncertainty
Semi-major axis	a (")	1.06	0.02
Eccentricity	e	0.766	0.004
Inclination	i ($^\circ$)	39	2
Ascending node	Ω ($^\circ$)	41	2
Longitude of pericenter	ω ($^\circ$)	116	2
Date of pericenter passage	T (yr)	1997.62	0.05
Period	P (yr)	56.3	0.1
Total mass	$M_{\text{tot}} (M_\odot)$	1.4	0.1

provide crucial information on the disk location, stability and dynamics.

This paper is laid out as follows. We first consider the stellar and orbital properties of the 99 Her system, including the possibility of a third component. Then we consider the *Herschel* image data and several different models that can explain it. Finally, we discuss the implications of these models for the formation of the system.

2 99 HERCULIS

The binary 99 Herculis (HD 165908, HIP 88745, GJ 704AB, ADS 11077) contains the 37th closest F star primary within the volume limited Unbiased Nearby Stars sample (Phillips et al. 2010). The Catalogue of Components of Doubles and Multiple systems (CCDM J18071+3034, Dommanget & Nys 2002) lists three components, but using Hipparcos proper motions Phillips et al. (2010) find that the 93" distant C component is not bound to the system. The binary pair has been known since 1859, and consists of an F7V primary orbited by a K4V secondary. The primary is known to be metal poor with $[\text{Fe}/\text{H}] \approx -0.4$ (e.g. Gratton et al. 1996; Adelman et al. 2000; Takeda 2007) and has an age consistent with the main-sequence (6 – 10Gyr from isochrone fitting, Nordström et al. 2004; Takeda 2007).

2.1 Binary Configuration

To interpret the *Herschel* observations requires an understanding of the binary configuration, which we address first. Typically, the important orbital elements in fitting binary orbits are the semi-major axis, eccentricity, and period, which yield physical characteristics of the system (if the distance is known). Regular observations of 99 Her date back to 1859 and the binary has completed nearly three revolutions since being discovered. Additional observations since the previous orbital derivation (Söderhjelm 1999), have allowed us to derive an updated orbit. Aside from a change of 180° in the ascending node (based on spectroscopic data Abt & Willmarth 2006), the orbital parameters have changed little; the main purpose of re-deriving the orbit is to quantify the uncertainties.

The orbit was derived by fitting position angles (PAs) and separations (ρ) from the Washington Double Star catalogue

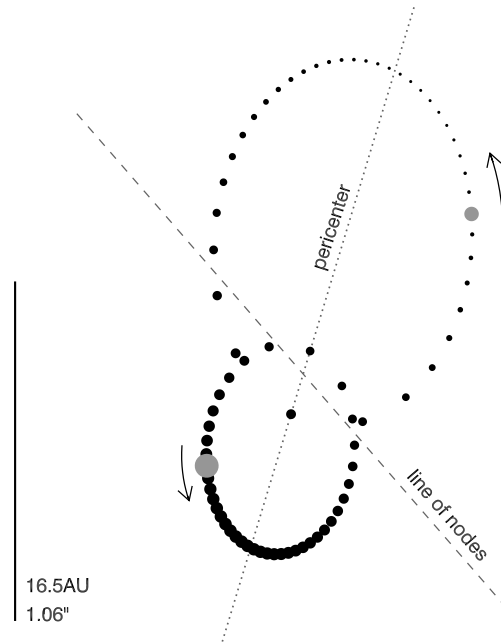


Figure 1. 99 Her binary orbit as seen on the sky, with the line of nodes and pericenter indicated. North is up and East is left. The stellar orbits are shown over one (anti-clockwise) orbital period with black dots. Grey dots (primary is the larger grey dot) show the positions at the PACS observation epoch. Black dot sizes are scaled in an arbitrary way such that larger dots are closer to Earth. The arrows indicate the direction of motion and the scale bar indicates the binary semi-major axis of $1.06''$ (16.5AU).

(Mason et al. 2011).² We included three additional observations; a *Hubble Space Telescope* (HST) *Imaging Spectrograph* (STIS) acquisition image (epoch 2000.84, $PA = 264 \pm 2^\circ$, $\rho = 0.54 \pm 0.02''$, Boesgaard et al. 2004), an adaptive optics image taken using the Lick Observatory Shane 3m telescope with the IRCAL near-IR camera as an ongoing search for faint companions of stars in the UNS sample (epoch 2009.41, $PA = 309 \pm 2^\circ$, $\rho = 1.12 \pm 0.02''$), and a Keck II NIRC2 L' speckle image taken to look for a third companion (see §2.2, epoch 2011.57, $PA = 317 \pm 1^\circ$, $\rho = 1.20 \pm 0.014''$). For visual data we set uncertainties of 7° to PAs and $0.5''$ to separations, for *Hipparcos* data we used 5° and $0.1''$, and for speckle observations without quoted uncertainties we used 2° and $0.04''$. The resulting orbital elements, shown in Table 1, vary only slightly from those derived by Söderhjelm (1999).³ The best fit yields $\chi^2 = 190$ with 399 degrees of freedom. The fit is therefore reasonable, and most likely the χ^2 per degrees of freedom is less than unity because the uncertainties assigned to the visual data are too conservative. If anything, the uncertainties quoted in Table 1 are therefore overestimated. However, visual data can have unknown systematic uncertainties due to individual observers and their equipment so we do not modify them (Hartkopf et al. 2001).

These data also allow us to derive a total system mass of $1.4M_\odot$, where we have used a distance of 15.64pc

² <http://ad.usno.navy.mil/wds/>

³ A figure showing the Söderhjelm (1999) orbit is available in the WDS catalogue.

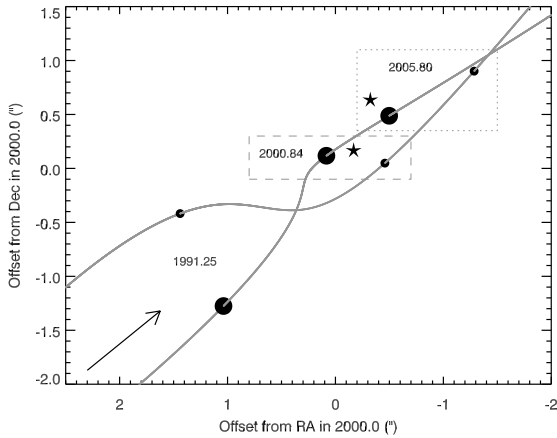


Figure 2. Motion of the 99 Her system (filled dots) in sky coordinates at three epochs. The epochs including the putative third component are enclosed in boxes. The arrow shows the direction of the system center of mass movement and the distance travelled in 5 years, and the grey lines show the path traced out by each star. Star symbols show the position of the third object observed in the STIS data in 2000 (dashed box) and by Scardia et al. (2008) in 2005 (dotted box).

(van Leeuwen 2008). While the total mass is well constrained by visual observations, the mass ratio must be derived from either the differential luminosity of each star or radial velocities. We use the spectroscopic mass function derived by Abt & Willmarth (2006), yielding a mass ratio of 0.49, which has an uncertainty of about 10%. The mass ratio from the differential luminosity is 0.58, with a much larger (20%) uncertainty (Söderhjelm 1999). Using the spectroscopic result, the primary (GJ 704A) has a mass of $0.94M_{\odot}$, while the secondary (GJ 704B) is $0.46M_{\odot}$.

The system configuration is shown in Figure 1 and is inclined such that the primary is currently closer to Earth than the secondary. The position of the B component relative to A on the date it was observed by *Herschel* in late April 2010 was $PA=314^{\circ}$ at an observed separation of $1.15''$ (22.6AU when de-projected), indicated by grey circles in the Figure.

2.2 A Third Component?

While the STIS images clearly resolve the binary, there is a possible third component with $PA \approx 284^{\circ}$ and $\rho \approx 0.27''$ that is about 2.4 times as faint as the B component. Scardia et al. (2008) also report a third component (epoch 2005.8) at $PA \approx 50^{\circ}$ and $\rho \approx 0.228''$ (no magnitude is given). However, while they detected the secondary again in mid-2007, they do not report any detection of the putative tertiary (Scardia et al. 2010). The detected positions are shown as star symbols in sky coordinates in Figure 2, which shows the motion of the 99 Her system. The system proper motion is $\mu_{\alpha} \cos \delta = -110.32 \text{ mas yr}^{-1}$, $\mu_{\delta} = 110.08 \text{ mas yr}^{-1}$ (van Leeuwen 2007), and accounts for the motion of the primary assuming the orbit derived in Söderhjelm (1999), which is very similar to ours. The small proper motion uncertainty means STIS and Scardia et al. (2008) cannot have seen the same object if it is fixed on the sky. There is no clear sign of a third component in the residuals from fitting the orbit of the secondary.

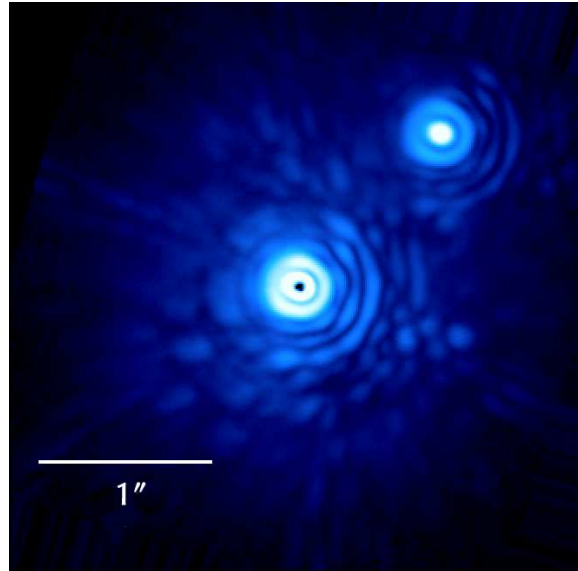


Figure 3. Keck/NIRC2 adaptive optics image of 99 Her at $3.8\mu\text{m}$, cropped to about $1.5''$ around the primary. North is up and East is left. The saturated A component is at the center of the frame.

To try and resolve this issue we obtained an adaptive optics image of 99 Her at L' ($3.8\mu\text{m}$) using the NIRC2 camera at Keck II on July 27, 2011, shown in Figure 3. We adopted the narrow camera (10 mas/pixel) and used a five-point dither pattern with three images obtained at each position consisting of 25 coadds of 0.181 seconds integration. The cumulative integration time for the final co-registered and coadded image is 67.875 seconds. The core of the A component point-spread-function is highly saturated, which degrades the achievable astrometry. We estimate the position of 99 Her A by determining the geometric center of the first diffraction ring. The position of 99 Her B is taken from the centroid of the unsaturated core. The PA and separation are quoted above.

There is no detection of the putative 99 Her C within $1.6''$ of the primary in the combined image if it is only a factor 2.4 fainter than the B component, because it would appear 20 times brighter than the brightest speckles. However, if it were closer to the primary than $0.2''$ it would currently be too close to detect. If the object was fixed on the sky near either the 2000 or 2005 locations, it would have been detected in the individual pointings of the five-point dither since each NIRC2 pointing has a field of view of $10'' \times 10''$. To be outside the field of view and still bound to the primary, the tertiary must have an apocenter larger than about 75AU ($5''$). An object in such an orbit would have a period of at least 200 years, so could not have been detected near the star in 2005 and be outside the NIRC2 field of view in 2011.

The non-detections by Scardia et al. (2010) and NIRC2 make the existence of the tertiary suspicious. It is implausible that the object was too close to, or behind the star both in 2007 and 2011, because at a semi-major axis of $0.23''$ (3.5AU) from the primary (similar to the projected separation) the orbital period is 7 years. Therefore, the object would be on opposite sides of the primary, and the two detections already rule out an edge-on orbit. Even assuming a circular orbit, such an object is unlikely to be dynamically stable, given the high eccentricity and

small pericenter distance (4.1AU) of the known companion. A tertiary at this separation would be subject to both short term perturbations and possible close encounters. If the mutual inclination were high enough, it would also be subject to Kozai cycles (Lidov 1962; Kozai 1962) due to the secondary that could result in a high eccentricity and further affect the orbital stability.

While it may be worthy of further detection attempts, the existence of this component appears doubtful and we do not consider it further.

3 IR AND SUB-MM DATA

3.1 Observations

Herschel Photodetector and Array Camera & Spectrometer (PACS, Poglitsch et al. 2010) data at 100 and 160 μm were taken in April 2010 during routine DEBRIS observations. Subsequently, a Spectral & Photometric Imaging Receiver (SPIRE, Griffin et al. 2010) observation was triggered by the large PACS excess indicating the presence of a debris disk and a likely sub-mm detection. The disk was detected, but not resolved with SPIRE at 250 and 350 μm . A 70 μm PACS image was later obtained to better resolve the disk. Because every PACS observation includes the 160 μm band, we have two images at this wavelength, which are combined to produce a single higher S/N image. All observations were taken in the standard scan-map modes for our survey; mini scan-maps for PACS data and small maps for SPIRE. Data were reduced using a near-standard pipeline with the *Herschel* Interactive Processing Environment (HIPE Version 7.0, Ott 2010). We decrease the noise slightly by including some data taken as the telescope is accelerating and decelerating at the start and end of each scan leg.

The high level of redundancy provided by PACS scan maps means that the pixel size used to generate maps can be smaller than the natural scale of 3.2"/pix at 70 and 100 μm and 6.4"/pix at 160 μm via an implementation of the “drizzle” method (Fruchter & Hook 2002). Our maps are generated at 1"/pix at 70 and 100 μm and 2"/pix at 160 μm . The benefit of better image sampling comes at the cost of correlated noise (Fruchter & Hook 2002), which we discuss below.

In addition to correlated noise, two characteristics of the PACS instrument combine to make interpretation of the data challenging. The PACS beam has significant power at large angular scales; about 10% of the energy lies beyond 1 arcminute and the beam extends to about 17 arcminutes (1000 arcsec). While this extent is not a problem in itself, it becomes problematic because PACS data are subject to fairly strong $1/f$ (low frequency) noise and must be high-pass filtered. The result is that a source will have a flux that is 10-20% too low because the “wings” of the source were filtered out. While this problem can be circumvented with aperture photometry using the appropriate aperture corrections derived from the full beam extent, the uncorrected apertures typically used for extended sources will result in underestimates of the source flux.⁴

Here, we correct the fluxes measured in apertures for 99 Her based on a comparison between PSF fitted and aperture corrected measurement of bright point sources in the DEBRIS

survey with predictions from their stellar models (based on the calibration of Rieke et al. 2008). These upward corrections are $16 \pm 5\%$, $19 \pm 5\%$, and $21 \pm 5\%$ at 70, 100, and 160 μm respectively. These factors depend somewhat on the specifics of the data reduction, so are *not* universal. This method assumes that the correction for 99 Her is the same as for a point source, which is reasonable because the scale at which flux is lost due to filtering the large beam is much larger than the source extent. The corrected PACS measurement is consistent with MIPS 70 μm , so we do not investigate this issue further.

The beam extent and filtering is also important for resolved modelling because the stellar photospheric contribution to the image is decreased. Therefore, in generating a synthetic star+disk image to compare with a raw PACS observation, the stellar photospheric flux should be decreased by the appropriate factor noted above. Alternatively, the PACS image could be scaled up by the appropriate factor and the true photospheric flux used.

Table 2 shows the measured star+disk flux density in each *Herschel* image. Uncertainties for PACS are derived empirically by measuring the standard deviation of the same sized apertures placed at random image locations with similar integration time to the center (i.e. regions with a similar noise level).

The SPIRE observations of 99 Her are unresolved. The disk is detected with reasonable S/N at 250 μm , marginally detected at 350 μm , and not detected at 500 μm . Fluxes are extracted with PSF fitting to minimise the contribution of background objects. Because all three bands are observed simultaneously (i.e. a single pointing), the PSF fitting implementation fits all three bands at once. A detection in at least one band means that all fluxes (or upper limits) are derived at the same sky position.

Additional IR data exist for 99 Her, taken with the Multi-band Imaging Photometer for *Spitzer* (MIPS, Rieke et al. 2004). Only the star was detected at 24 μm ($270.3 \pm 0.1\text{mJy}$), but this observation provides confirmation of the 99 Her stellar position in the PACS images relative to a background object 1.8 arcmin away to the SE ($PA = 120^\circ$) that is visible at 24, 70, and 100 μm . The presence of an excess at 70 μm ($98 \pm 5\text{mJy}$ compared to the photospheric value of 30mJy) was in fact reported by Koerner et al. (2010). They did not note either the circumbinary nature or that the disk may be marginally resolved by MIPS at 70 μm . Because our study focuses on the spatial structure, we use the higher resolution PACS data at 70 μm , but include the MIPS data to model the SED.

3.2 Basic image analysis

Figure 4 shows the *Herschel* PACS data. Compared to the beam size, the disk is clearly resolved at all three wavelengths. At 160 μm the peak is offset about 5" East relative to both the 70 and 100 μm images. However, the disk is still visible at 160 μm as the lower contours match the 70 and 100 μm images well. The 160 μm peak is only 2-3 σ more significant than these contours. While such variations are possible due to noise, in this case the offset is the same in both 160 μm images, so could be real. The fact that the peak extends over several pixels is not evidence that it is real, because the pixels in these maps are correlated (see below). If real, this component of the disk or background object cannot be very bright at SPIRE wavelengths because the measured fluxes appear consistent with a blackbody fit to the disk

⁴ See <http://herschel.esac.esa.int/twiki/bin/view/Public/WebHome> for details regarding the PACS beam extent and calibration.

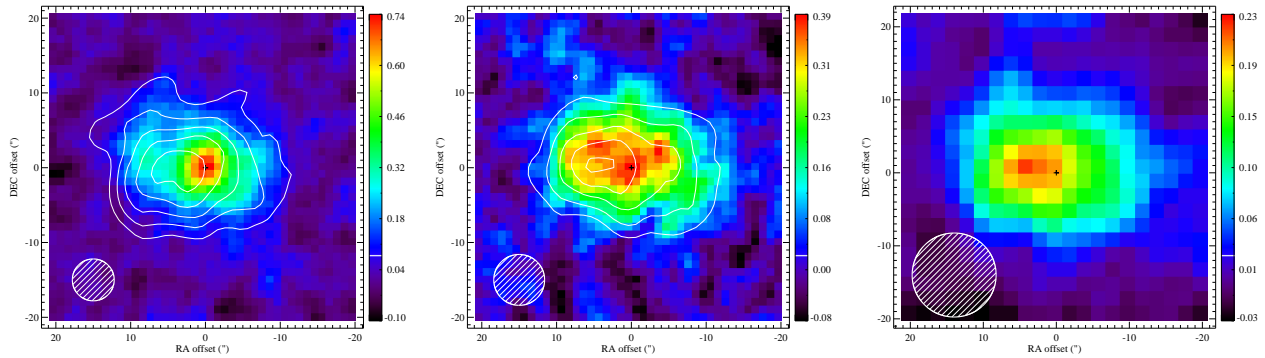


Figure 4. *Herschel* PACS images of the 99 Her system at $70\mu\text{m}$ (left) $100\mu\text{m}$ (center) and combined $160\mu\text{m}$ (right). North is up and East is left. Colour bars show levels in units of $\text{mJy}/\text{arcsec}^2$. Contours in the left two panels show the $160\mu\text{m}$ data from each observation in 5 levels from $3-9\sigma$. The images are centered on the primary position (plus symbol) derived from the $70\mu\text{m}$ image. Hatched circles show the FWHM beam sizes of $5.6''$, $6.8''$, and $11.5''$ at 70 , 100 , and $160\mu\text{m}$ respectively.

Table 2. *Herschel* photometry of 99 Her. The disk is not detected at $500\mu\text{m}$ and can be considered a 3σ upper limit of 24mJy .

Band	Flux (mJy)	Uncertainty	Method
PACS70	93	10	$15''$ aperture
PACS100	87	10	$15''$ aperture
PACS160	80	15	$17''$ aperture
SPIRE250	44	6	PSF fit
SPIRE350	22	7	PSF fit
SPIRE500	4	8	PSF fit

(see §4). Based on an analysis of all DEBRIS maps (that have a constant depth), the chance of a 3σ or brighter background source appearing within $10''$ of 99 Her at $160\mu\text{m}$ is about 5% (Thureau et al in prep). Given that the $160\mu\text{m}$ offset is only a $2-3\sigma$ effect (i.e. could be a $2-3\sigma$ background source superimposed on a smooth disk), the probability is actually higher because the number of background sources increases strongly with depth. These objects have typical temperatures of $20-40\text{K}$ (e.g. Amblard et al. 2010), so could easily appear in only the $160\mu\text{m}$ image, particularly if the disk flux is decreasing at this wavelength.

We now analyse the PACS images using 2D Gaussian models to estimate the disk size, inclination, and position angle. A 2D Gaussian fits the star-subtracted PACS $100\mu\text{m}$ image fairly well, with major and minor full-width half-maxima of 17.7 and $12.8''$ at a position angle of 78° . Quadratically deconvolving from the $6.7''$ FWHM beam assuming a circular ring implies an inclination of 48° from face-on and an estimated diameter of 250AU . Gaussian fitting to star-subtracted images at both 70 and $160\mu\text{m}$ yields similar results.

As noted above, estimation of uncertainties in these parameters is non-trivial due to correlated noise, but made easier by the constant depth of our survey. By inserting the best fit Gaussian to the star-subtracted image of the 99 Her disk from the $100\mu\text{m}$ image into 438 other $100\mu\text{m}$ maps at high coverage positions offset from the intended target, we obtain a range of fit parameters for hundreds of different realisations of the same noise. This process yields an inclination of $45 \pm 5^\circ$ and PA of $75 \pm 8^\circ$. Repeating the process, but using the best fit Gaussian for the $70\mu\text{m}$ image yields an inclination of $44 \pm 6^\circ$ and PA of $68 \pm 9^\circ$. Though the inclination of the disk is similar to the bi-

nary, the position angle is significantly different from the binary line of nodes of $41 \pm 2^\circ$. This difference means that the disk and binary orbital planes are misaligned.

As a check on the above approach, we can correct for the correlated noise directly. Fruchter & Hook (2002) show that for a map that has sufficiently many dithers (corresponding in our case to many timeline samples across each pixel), a noise ‘‘correction’’ factor of $r/(1 - 1/3r)$ can be derived, where r is the ratio of natural to actual pixel scales and is 3.2 for our PACS maps. A correction factor of 3.6 for the measured pixel to pixel noise is therefore required when estimating the uncertainty on a fitted Gaussian. Including this factor at $70\mu\text{m}$ and calculating the uncertainty by the standard $\Delta\chi^2$ method yields an inclination of $42 \pm 7^\circ$ and a PA of $68 \pm 9^\circ$. At $100\mu\text{m}$ the result is an inclination of $44 \pm 6^\circ$ and a PA of $76 \pm 8^\circ$. These results are therefore almost exactly the same as the empirical method used above and therefore lead to the same conclusion of misalignment.

As will become apparent in §5, there is reason to believe that the disk plane could be perpendicular to the binary pericenter direction. The projection of the binary pericenter direction on the sky plane has a PA of $163 \pm 2^\circ$, and a line perpendicular to this has a PA of $73 \pm 2^\circ$. Therefore, the observed disk position angle of about 72° is consistent with being at 90° to the binary pericenter direction.

4 SED

The combination of all photometry for 99 Her allows modelling of the spectral energy distribution (SED). The model is separated into two components; a stellar atmosphere and a disk. Due to being fairly bright ($V \sim 5\text{mag}$) the system is saturated in the 2MASS catalogue. However, sufficient optical photometry for each individual star and the pair exists (Henry & McCarthy 1993; Hauck & Mermilliod 1997; Perryman & ESA 1997; Mermilliod 2006), as well as infrared measurements of the AB pair from AKARI and IRAS (Moshir & et al. 1990; Ishihara et al. 2010). These data were used to find the best fitting stellar models via χ^2 minimisation. This method uses synthetic photometry over known bandpasses and has been validated against high S/N MIPS $24\mu\text{m}$ data for

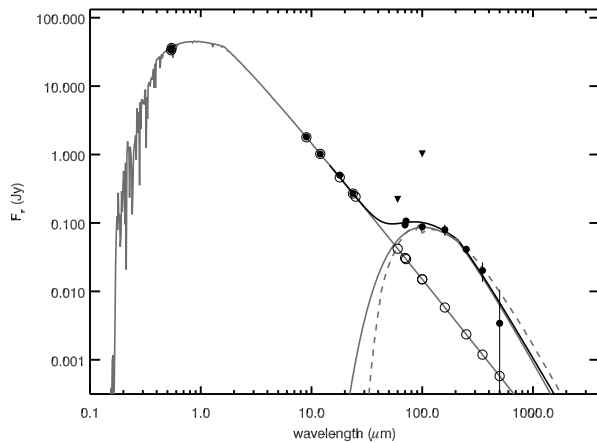


Figure 5. SED for the 99 Her system (both stars) showing the stellar and disk models (grey lines) and star+disk model (black line). The blackbody disk model is the solid grey line, and the physical grain model the dashed line. Photometric measurements are shown as black filled circles, and synthetic photometry of the stellar atmosphere as open circles ($U - B$, $B - V$, & $b - y$ colours, and $m1$ and $c1$ Stromgren indices were fitted but are not shown here). Black triangles mark upper limits from IRAS at 60 and 100 μm .

DEBRIS targets, showing that the photospheric fluxes are accurate to a few percent for AFG-type stars. The stellar luminosities ($L_{\star,A} = 1.96L_{\odot}$, $L_{\star,B} = 0.14L_{\odot}$) and IR fluxes of the individual components are consistent with the fit for the pair ($L_{\star,AB} = 2.08L_{\odot}$). The fit for the AB pair is shown in Figure 5.

The spatial structure of the disk can be modelled with dust at a single radial distance of 120AU (i.e. thin compared to *Herschel's* resolution, §5), so disk SED modelling can be decoupled from the resolved modelling once this radial distance is known. Because we have measurements of the disk emission at only five wavelengths, we cannot strongly constrain the grain properties and size distribution. We fit the data with a blackbody model, and then compare the data with several “realistic” grain models (Li & Greenberg 1997; Augereau et al. 2001; Wyatt & Dent 2002).

In fitting a blackbody we account for inefficient grain emission at long wavelengths by including parameters λ_0 and β , where the blackbody is modified by a factor $(\lambda_0/\lambda)^\beta$ for wavelengths longer than λ_0 . The best fitting model has a temperature of 49K and fractional luminosity $L_{\text{disk}}/L_{\star} = 1.4 \times 10^{-5}$. The SPIRE data are near the confusion limit of about 6mJy, so the parameters β and λ_0 are unconstrained within reasonable limits by the data (based on previous sub-mm detections for other disks we fix them to $\lambda_0 = 210\mu\text{m}$ and $\beta = 1$ in Figure 5 (Wyatt et al. 2007b)).

Assuming that grains absorb and emit like blackbodies, the radial dust distance implied by 49K is 45AU. Because the disk is observed at a radius of 120AU (i.e. is warmer than expected for blackbodies at 120AU), the dust emission has at least some contribution from grains small enough to emit inefficiently in the 70-350 μm wavelength range. Because the SED alone is consistent with a pure blackbody (i.e. with $\beta = 0$), we cannot make such a statement without the resolved images. However, actually constraining the grain sizes is difficult because temperature

and emission are also affected by composition. We fit the data by generating disk SEDs for grains at a range of semi-major axes and choosing the one with the lowest χ^2 . If the dust semi-major axis is different from the observed semi-major axis of 120AU the model parameters are changed and the model recalculated, thus iterating towards the best fit.

We model the dust with a standard diameter (D) distribution $n(D) \propto D^{2-3q}$ where $q = 1.9$ (equivalently $n(M) \propto M^{-q}$ where M is mass O’Brien & Greenberg 2003), with the minimum size set by the blowout limit for the specific composition used (about 1.4 μm) and a maximum size of 10cm. The size distribution probably extends beyond 10cm, but objects larger than 10cm contribute negligibly to the emission because the size distribution slope means that smaller grains dominate. Preliminary tests found that icy grains provided a much better fit than silicates. To refine the grain model so the SED and resolved radius agree, we introduced small amounts of amorphous silicates to the initially icy model. The grains are therefore essentially ice mixed with a small fraction ($f_{\text{sil}} = 1.5\%$) of silicate. The icy grain model is shown as a dotted line in Figure 5. This model has a total dust surface area of 14AU² and a mass of order 10 M_{\oplus} if the size distribution is extrapolated up to 1000km size objects.

The parameters from this model are degenerate for the data in hand; for example the size distribution could be shallower and the fraction of silicates higher (e.g. $q = 1.83$ and $f_{\text{sil}} = 4\%$). If we allow the minimum grain size to be larger than the blowout limit, the disk is well fit by amorphous silicate grains with $q = 1.9$ and $D_{\text{bl}} = 10\mu\text{m}$. The disk spectrum can even be fit with a single size population of 25 μm icy grains. However, the predictions for the flux at millimeter wavelengths depend on the size distribution, with lower fluxes for steeper size distributions. Therefore, grain properties and size distribution can be further constrained in the future with deep (sub)mm continuum measurements.

In summary, it is hard to constrain the grain sizes or properties. There is a difference in the required minimum grain size that depends on composition. Because icy grains are reflective at optical wavelengths, a detection of the disk in scattered light could constrain the albedo of particles, and therefore their composition.

5 SPATIAL STRUCTURE

The PACS images of the 99 Her disk are resolved, which allows modelling of the spatial distribution of grains that contribute to the observed emission at each wavelength. We compare synthetic images with the *Herschel* observations in several steps: i) Generate a three dimensional distribution of surface area $\sigma(r, \theta, \phi)$, where the coordinates are centered on the primary star. ii) Generate a radial distribution of grain emission properties. Because the SED can be modelled with blackbody grains at 49K and the spatial structure modelled with a narrow ring, there is no real need for a radial temperature dependence and the grain properties are only a function of wavelength: $P(\lambda) = B_{\nu}(49K, \lambda)$. Practically, we use a radial temperature dependence $T \propto r^{-1/2}$ centered on the primary, normalised so that the disk ring temperature is 49K. This approach ensures that temperature differences due to non-axisymmetries (negligible for 99 Her) are automatically taken into account. iii) Generate a high resolution model as viewed from a specific direction. The emission in a single pixel of angular size x from a single vol-

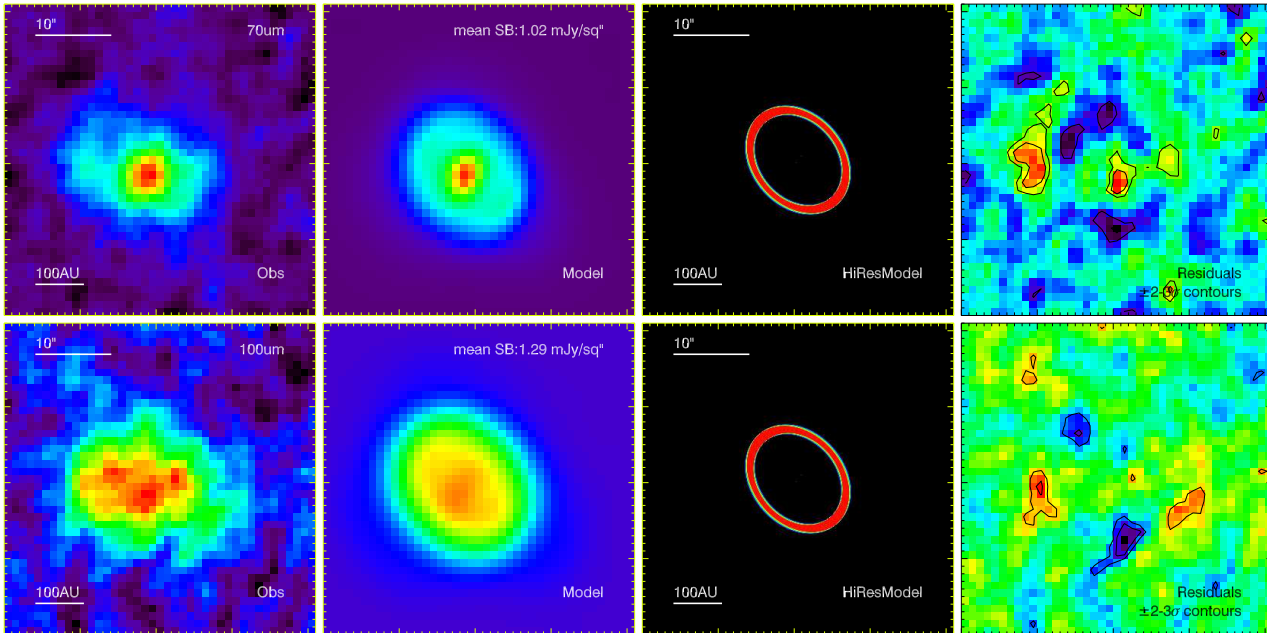


Figure 6. Simple ring model where the disk is aligned with the binary orbital plane, compared to the PACS 70 (top row) and 100 μm (bottom row) observations. North is up and East is left. Columns show the data, model convolved with the PACS beam, a high resolution model, and the data-model residuals from left to right. The model includes stellar photospheric fluxes, which lie in two pixels near the ring center but are not visible in the high resolution plot. In the residual plots, contours show ± 2 and 3σ in units of pixel to pixel RMS.

ume element in the three dimensional model dV viewed along a vector \mathcal{R} is $dF_\nu(\lambda, r, \theta, \phi) = P(\lambda)\sigma(r, \theta, \phi)dV$, where $dV = x^2 d^2 d\mathcal{R}$, so $d\mathcal{R}$ is the length of the volume element, and d is the distance to the particles from Earth (Wyatt et al. 1999). The emission is derived by integrating along the line of sight \mathcal{R} for each pixel in the synthetic image. The photospheric fluxes for each star (decreased by the factors noted in §3.1) are placed in the relevant pixels at this step. iv) Convolve the high resolution model with a high resolution telescope+instrument beam, for which we use interpolated and rotated PACS images of the star Arcturus.⁵ v) Degrade the resolution to match the data. vi) Generate a map of residuals, defined by $(\text{observed} - \text{model})/\text{uncertainty}$, where the uncertainty is the pixel to pixel RMS for that observation. We compute the model χ^2 from pixels in a square crop around the disk.

A minor consideration is that in the general circumbinary case the disk temperature is not axisymmetric because the disk orbits the center of mass, not the primary. An axisymmetric disk is therefore subject to a temperature asymmetry such that it will be slightly hotter, and therefore brighter, where the distance to the primary is smallest. This “binary offset” asymmetry will rotate with the primary, and will be most pronounced in the coplanar case. The result of this effect is similar to the offset caused by perturbations from an eccentric object (“pericenter glow” Wyatt et al. 1999). However, the pericenter glow is offset towards the pericenter of the perturbing object, so does not rotate unless the perturbing object’s pericenter precesses. The offset from the primary and the pericenter glow are completely

⁵ The observations are reduced in sky coordinates, so the spacecraft orientation is different for each observation and the PSF must be rotated accordingly. This rotation step could be avoided by reducing both in spacecraft coordinates.

independent effects. Therefore, if the pericenter glow effect is present, it will reinforce and cancel the binary offset effect, depending on the relative magnitude of each each offset. The magnitude of the binary offset effect is negligibly small ($\lesssim 1\%$) because the disk radius is much larger than the binary separation. Because our model is centered on the system center of mass this effect is taken into account anyway. We discuss the effect of the binary on pericenter glow in §5.1.1.

To fit the data requires a handful of parameters, some are required for all models and some are model specific. The disk surface area, temperature, radius, width, and total opening angle are the five physical parameters for a ring. The sky position angle and inclination are two further parameters that set the orientation, but can be fixed if the disk plane is assumed to be aligned with the binary. In addition each observation has the stellar RA and Dec as parameters to allow for the $2''$ 1σ pointing accuracy of *Herschel*. The position at 160 μm is tied to the 100 μm position. There are therefore eleven possible parameters to fit for the resolved observations at 70, 100, and 160 μm . We fix the disk temperature to 49K in all cases.

From the basic analysis (§3.2), a simple ring coplanar with the binary does not appear a viable option. To emphasise this point we show 70 and 100 μm images of the best fitting coplanar model in Figure 6. This model was generated by the steps outlined above, and the rightmost three panels are the results of steps iv (convolved model), iii (high resolution model), and vi (residuals). We fix the disk width to 20AU, the opening angle to 5° , and the position angle and inclination to the binary plane, so there are six free parameters (surface area, radius, and two pairs of RA/Dec sky positions). While we include the 160 μm data in the fitting, it does not constrain the fit strongly due to low S/N and always shows $\sim 2\sigma$ residual structure due to the offset peak. For comparison with the models below, the χ^2 value

for all three PACS bands is 4278 with 3797 degrees of freedom. The positive and negative residuals (rightmost panels) show that the disk ansae in the model have the wrong orientation at both wavelengths. It is clear that any structure symmetric about the binary line of nodes will not be consistent with the observations because the position angle is significantly different.

An alternative explanation for the misalignment between the observed position angle and the binary line of nodes could be that the dust does in fact lie in the binary plane, but that the particles are on eccentric orbits with common pericenter directions (i.e. the disk is elliptical and offset from the binary). In principle, the observations can constrain the eccentricity and pericenter direction. However, this model fails because the eccentricity needed to match the observed position angle is too extreme. In order to obtain an ellipse that lies in the binary orbital plane and has a position angle and aspect ratio similar to the observations requires eccentricities $\gtrsim 0.4$. The eccentricity of these particles is so high that i) the ring is significantly offset from the star and ii) the ring has an extreme pericenter glow asymmetry at all wavelengths caused by particles residing at different stellocentric distances. Because the PACS $70\mu\text{m}$ image shows that the star lies very near the disk center, such a strong offset is ruled out.

We now consider two relatively simple models that account for the misalignment between the disk and binary orbital planes. The first is based on the expected secular evolution of circumbinary particles, and the second is a simple misaligned ring where the disk position angle and inclination are free parameters.

5.1 Secularly perturbed polar ring

In this section we consider a ring inspired by the secular evolution of circumbinary particles. This approach ensures that the disk is stable over the stellar lifetime and encompasses the particle dynamics dictated by the binary. We first outline the dynamics of circumbinary particles, and then show the model for the 99 Her disk.

5.1.1 Dynamics

Particle dynamics are important for evolution and stability in the 99 Her system. A circumbinary disk will have its inner edge truncated, while circumstellar disks around either component can be truncated at their outer edges. In addition, secular perturbations lead to precession of test particles' nodes coupled with inclination variations. We explore these dynamics using the *Swift HJS* integrator (Beust 2003).

In general, disk truncation allows us to place limits on possible locations for disk particles. However, in the case of 99 Her there is no evidence for disk components orbiting only one star, and the apparent circumbinary disk extent lies well beyond $\sim 30\text{--}60\text{AU}$ stability limit at any inclination (Wiegert & Holman 1997; Doolin & Blundell 2011).

Circumbinary particles also undergo long-term dynamical evolution due to secular perturbations. Because the binary has a small mass ratio and high eccentricity, the dynamics are not well described by the circular restricted three-body problem, commonly applied in the case of debris disks perturbed by planets. Similar dynamics have previously been explored in the context of the HD 98800 system (Verrier & Evans 2008, 2009)

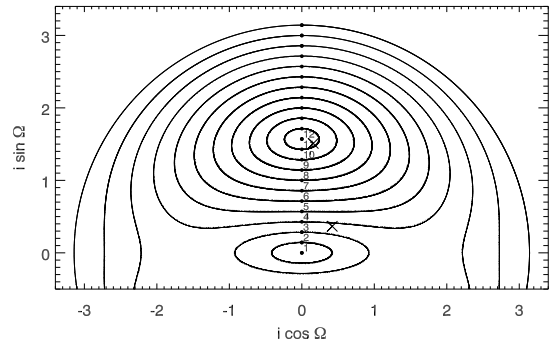


Figure 7. Secular evolution of circumbinary particles in inclination (i) and line of nodes (Ω) space. Particles begin at dots and move along the curves due to perturbations from the binary. Particles that would appear reflected in the x axis duplicate the spatial distribution so are not shown. Crosses show the current location of particles in the two interpretations of the transient ring model (§5.2). Over time these particles will sweep out curves similar to particles 4 and 11. The long term structure of the transient ring will therefore appear similar to either panel 4 or 11 in Figure 8, depending on which inclination is correct.

and more generally (Farago & Laskar 2010; Doolin & Blundell 2011).

These studies show that the inclination (i) and line of nodes (Ω) of circumbinary particles evolve due to perturbations from the binary. Depending on the binary eccentricity and particle inclination, Ω can circulate (increase or decrease continuously) or librate (oscillate about 90° or 270°). Particles with low inclinations stay on low inclination orbits, thus sweeping out a roughly disk or torus-like volume over long timescales. Higher inclination particles are subject to nodal libration and large inclination variations, thus sweeping out large parts of a sphere around the binary. Most importantly for 99 Her, the orbits of particles with $\Omega \approx 90^\circ$ (or 270°) and on near polar orbits will not change much due to secular evolution, thus sweeping out a polar ring.

Figure 7 shows the secular evolution of 23 particles on initially circular orbits in complex inclination space. All particles have initial nodes of 90° relative to the binary pericenter and inclinations spread evenly between 0 and 180° and are integrated for 1Gyr (i.e. there are no other significant effects on such long timescales). At 120AU, the time taken for a particle to complete one cycle of secular evolution (make a loop in figure 7) varies in the range $2\text{--}7 \times 10^5$ years, with larger loops taking longer. These times will also scale with particle semi-major axis. Particles 1–12 are those with initial inclinations between $0\text{--}90^\circ$ that are sufficient to describe the range of spatial structures as we cannot distinguish between pro/retrograde orbits.

The particles can be split into two groups; those with low inclinations whose nodes circulate (1–3) and those with high inclinations whose nodes librate about 90° (4–12). The dividing line (separatrix) between these families for the binary eccentricity of 0.76 is 21° when $\Omega = 90^\circ$ (or 270° , Farago & Laskar 2010). While particles in the first group have $i < 21^\circ$ when $\Omega = 90^\circ$, their inclinations when $\Omega = 0^\circ$ (or 180°) can be as high as 90° . Thus, particles near the separatrix will sweep out an entire spherical shell during their secular evolution. Similarly, particles near the separatrix but in the second group also

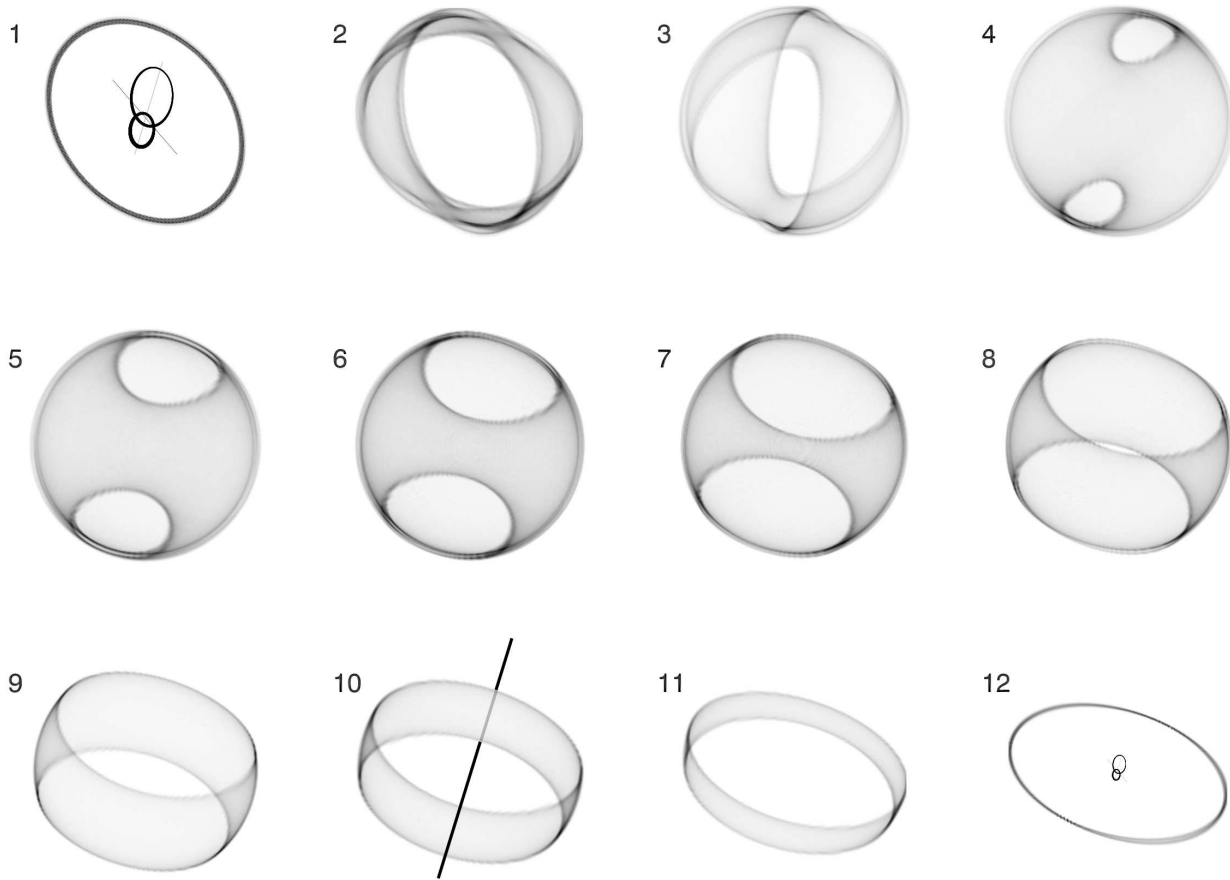


Figure 8. Debris structures derived from the secular evolution of particles 1-12 in Figure 7 as they would be seen in the 99 Her system. In panels 1 and 12 we have included the binary orbit from Figure 1. The orbit is not to scale in panel 1 for better visualisation, but is in panel 12. Panel 10 includes a line along the binary pericenter direction that is obscured by the ring to show the orientation. In panels 1-3 particles circulate and the binary orbital plane is the plane of symmetry. In panel 1, the coplanar case, the position angle of the disk is aligned with the line of nodes. In panel 3 the binary is nearly surrounded by a broad shell of particles. In panels 4-12 particles nodes librate and the plane of symmetry is perpendicular to the binary pericenter direction. In panels 7-12 the observed position angle is perpendicular to the binary pericenter.

sweep out a spherical shell, though the orbital evolution is different.

To visualise the structures swept out by these families of particles due to secular perturbations, Figure 8 shows the resulting debris structures for particles that follow each of the trajectories 1-12 from Figure 7 (left to right and down). The structures are oriented as they would be seen on the sky in the 99 Her system (i.e. have the same orientation with respect to the binary orbit shown in Figure 1). Each structure was generated by taking the relevant particle at each time step and spawning 1000 additional particles spread randomly around the orbit. This process was repeated for every time step, thus building up the spatial density of a family of particles that follow a specific curve in Figure 7. These structures are optically thin, which makes interpreting them somewhat difficult. We have included a scaled version of the binary orbit from Figure 1 in some panels in an attempt to make the orientations clearer.

The first (top left) panel shows a circular orbit coplanar with the binary. The PA is the binary line of nodes, and Figure 6 shows why a disk in the plane of the binary is not a satisfactory match to the observations. The second and third panels are still symmetric about the binary orbital plane, but have a wider range

of inclinations and are an even poorer match to the observations. Panel 3 shows that while particle inclinations are restricted for $\Omega = 90, 270^\circ$, they can be large for $\Omega = 0, 180^\circ$ and result in a “butterfly” structure when viewed down the binary pericenter direction.

The remaining panels are for particles 4-12, whose nodes librate and for which the plane of symmetry is perpendicular to the binary pericenter direction. In panel 4 the range of nodes and inclinations is so large that a particle sweeps out nearly an entire spherical shell during a cycle of secular evolution (i.e. the particle is near the separatrix). This range decreases as the initial inclination nears a polar orbit, at which point the orbital elements do not evolve and the resulting structure appears in panel 12 as a simple ring. The key difference from the ring in panel 1 is that this ring’s position angle is perpendicular to the sky projection of the binary pericenter direction, and as noted in §3.2 is therefore similar to the observed PA in the PACS images.

Secular perturbations from the binary also affect the long term evolution of particle eccentricities and pericenter longitudes. These effects are taken into account by our n -body approach. However, we noticed that the eccentricities imposed (“forced”) on the particles are lower than would be expected for

a lower mass companion. Further n -body simulations of coplanar particles show that for 99 Her with a mass ratio of 0.49 the forced eccentricity at 120AU is about 0.03, but if the mass ratio were 0.05 the forced e is 0.1.

This lack of significant eccentricity forcing is visible by its absence in Figure 8, where the structures would be much broader if there were a large range of particle eccentricities. For example, if the mass of the secondary in the 99 Her system were significantly smaller, the model in panel 1 would become broader and offset from the binary center of mass, resulting in a small pericenter glow effect.

This dependence suggests that a circumbinary disk’s structure may help constrain the binary mass ratio in cases where it is uncertain. However, we cannot apply this idea to make a better estimate of the 99 Her mass ratio because the PACS observations do not have enough resolution. In addition, at high inclinations the particle behaviour is more complicated, because polar particles switch between pro and retrograde orbits and do not follow simple circles in complex eccentricity space.

5.1.2 Polar ring model

We now use the models from Figure 8 to fit the PACS observations. The model has only seven free parameters; the particle semi-major axis and initial inclination, the surface area of dust, and the same four RA/Dec positions. The dust temperature is fixed to 49K. Using a semi-major axis of 120AU, each panel was compared to the PACS images, setting the surface area in grains for each model to obtain the least residual structure. Of these we found that panel 9 was the best fit, shown in Figure 9. These particles follow near-polar orbits so we call this model a “polar ring.” We find $\chi^2 = 3202$. In terms of χ^2 the results for panels 8 and 10 are similar, but slightly higher. The uncertainty in the initial inclination is therefore about 10° , and for the semi-major axis about 10AU. This model is much better than the coplanar model of Figure 6, with no overlapping residual structure at 70 and 100 μ m. The particles likely occupy a wider range of orbits than a single semi-major axis with some non-zero eccentricity, which may account from some minor (2σ) structure in the residuals at the disk ansae at 70 μ m. However, given that this model stems directly from the secular evolution, has very few free parameters, and accounts for the structure in all PACS images, we consider it a plausible explanation.

5.2 Transient ring model

A simple circular ring is a natural model to fit to the observations. This model has eight free parameters, with the width of the ring fixed at 20AU and the opening angle fixed to 5° . As expected from the simple analysis in §3.2 the position angle of this ring is not aligned with the binary line of nodes, and is therefore misaligned with the binary orbit.

The interpretation depends on the orientation of the best fit. A misaligned ring with polar orbits and the correct line of nodes would be considered further evidence in favour of the above polar ring model. A ring with a non-polar orientation will be spread into a broad structure like one of the panels in Figure 8 by secular perturbations. The ring cannot be long-lived and could therefore be the aftermath of a recent collision, seen after the collision products have sheared into a ring, but before secular

perturbations destroy the ring structure. Thus we call this model a “transient ring.”

This model is shown in Figure 10, and is a reasonable match to the PACS observations. However, the residuals at 70 μ m show that the ring produces a structure that is slightly too elliptical, compared to the more rectangular structure that is observed and reproduced by the polar ring. This model also has less emission at the stellar position than is observed. For this model $\chi^2 = 3304$. The disk is inclined 53° from face-on and the PA is 81° . The uncertainties are similar to those derived for the Gaussian fits in §3.2. The minimum relative inclination between the disk and binary orbital planes is therefore 32 degrees, with a line of nodes with respect to the binary orbit of 139° .

However, the inclination between the disk and binary plane could also be 87° if the disk were mirrored in the sky plane, which means that the particles have near-polar orbits. These orbits are nearly the same as panel 12 of Figure 8 (the narrow polar ring) because the line of nodes with respect to the binary orbit is 276° .

These two interpretations correspond to two points in Figure 7, shown as crosses. Over time the particles would spread around to make two more lines similar to those drawn. The particles in the lower inclination case are close to the separatrix, and would therefore sweep out a near-spherical shell like panel 4 of Figure 8. In this case, the long term evolution produces structures that have the wrong position angle and are a poor match to the observations. The higher inclination case is very nearly a polar ring and would look very similar to panel 11. Such a result is expected because we found above that the polar ring model works well, and argues in favour of the polar-ring interpretation.

We can in fact improve this simple ring model by increasing the total disk opening angle (i.e. allowing a larger range of inclinations), which emulates the range of inclinations that result from the secular evolution. We find a best fit when the particle inclinations are 25° (total opening angle of 50°), where $\chi^2 = 3210$. This model looks very similar to the preferred polar ring model above, but is not generated in the same way, and will therefore change somewhat due to secular perturbations over time because the disk is not perfectly polar.

6 DISCUSSION

We strongly favour the polar ring model as the best explanation of the disk structure surrounding 99 Her. The polar ring is stable for the stellar lifetime, and takes the secular dynamics into account. The transient ring model, where the disk orientation is not fixed, also finds that the disk particles can have polar orbits. However, because the ring could be mirrored in the sky plane and appear the same, the ring could be misaligned with the binary orbital plane by about 30° . Based on χ^2 and the residuals the polar ring is marginally preferable over the transient ring. However, given that a more realistic model with a range of particle radii and inclinations could improve the fit in each case, we do not assign much importance to the relatively small χ^2 differences. Instead, we consider several constraints on the collisional evolution that argue against the transient ring interpretation.

By considering the timescales for collisions and secular evolution, we can estimate the likelihood of observing the products of a collision as a transient ring before it is spread into a broader structure. Based on the observed radius and total cross-

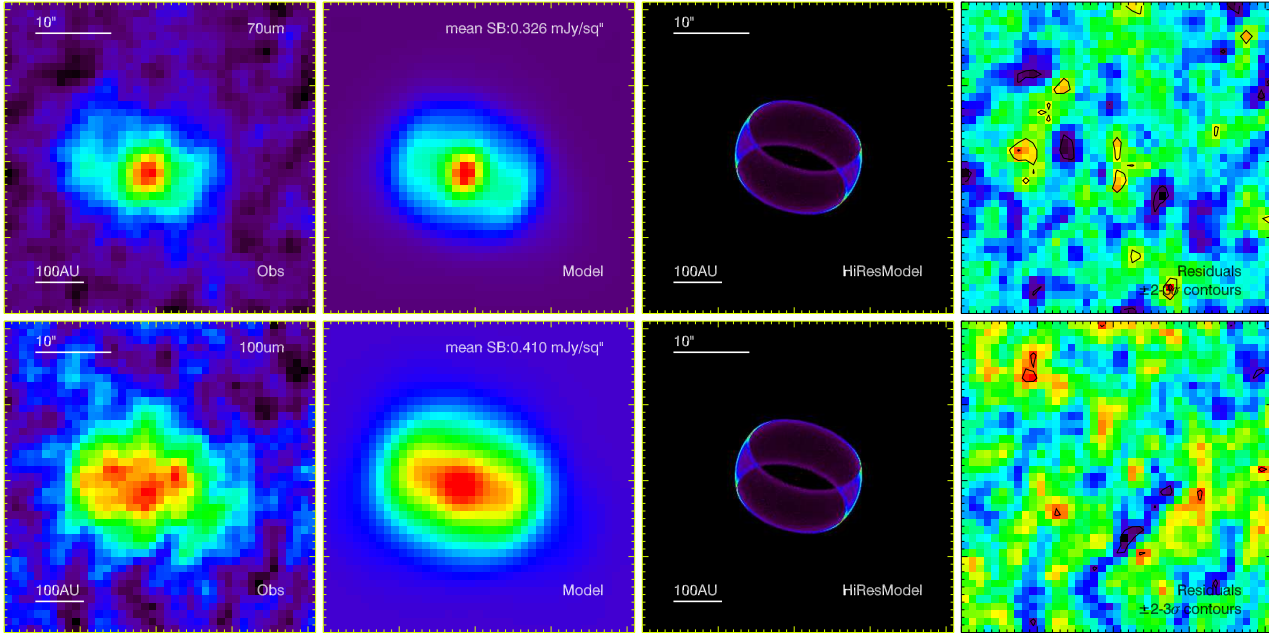


Figure 9. Polar ring model compared to the PACS 70 (top row) and $100\mu\text{m}$ (bottom row) observations. Layout is as for Figure 6.

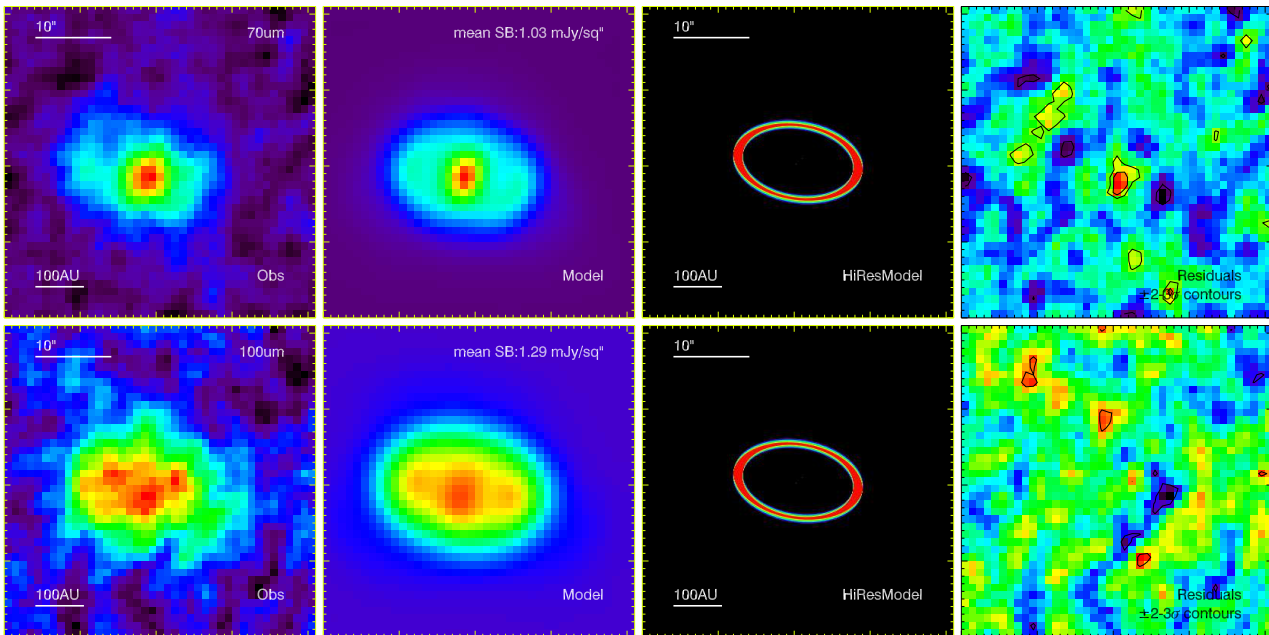


Figure 10. Transient ring model compared to the PACS 70 (top row) and $100\mu\text{m}$ (bottom row) observations. Layout is as for Figure 6.

sectional area, the collisional lifetime of grains just above the blowout size is about a million years (Wyatt et al. 2007a). The emission could last much longer if larger objects exist in the size distribution, and the lifetime scales with the maximum size as $\sqrt{D_{\text{max}}/D_{\text{bl}}}$, so depends on the size of the largest fragment created in the collision. If the largest fragments are at least 1mm in size the lifetime is at least 50Myr, and we would expect the collisional cascade to be detectable for this length of time. The secular precession timescale is about 0.5Myr, and it is reasonable to assume that the ring structure would be erased by secular

perturbations within 10 secular timescales. Thus, the collisional products would be observable as a ring for only 5Myr. Because the collision time is longer than the secular time, the collision products would spend at most a tenth of their lifetime appearing as a misaligned ring, and the remainder as a broader structure. That is, assuming such a collision did occur, we have less than

a 1:10 chance of observing the collision products as a ring that looks like the *Herschel* observations.⁶

While 1:10 is not unreasonable, this estimate does not consider the object that must be destroyed to generate the observed dust or the plausibility of a 1mm maximum size. To produce the observed fractional luminosity, a parent body of at least 600km in diameter must be broken into blowout sized grains. With the more realistic assumption that the collision produced a range of grain sizes, the parent body must be larger, about 2000km if grains were as large as the 1mm assumed above (assuming $q = 11/6$). Under the more realistic assumption of a wide range of fragment sizes, up to 1km say, the parent body would need to be roughly Earth-sized. However, for such large fragments the dust lifetime would be 50Gyr and the chance of observing the structure as a ring very unlikely (1:10,000).

We can estimate the ability of collisions to smash large objects into small pieces by considering their strength and possible collision velocities. The specific energy needed for catastrophic disruption, where the largest collision product is half the original mass (i.e. very large), is roughly 10^{11} erg/g for objects 2000km in size (Stewart & Leinhardt 2009). The energy needed to disrupt an object so that the collision products are all very small must be larger. The maximum collision energy possible for circular orbits is for a collision between two equal sized objects on pro and retrograde orbits. The collision energy assuming such an impact at twice the orbital velocity of a few km/s at 100AU is a few 10^{10} erg/g. Therefore, only in the most optimistic (highest velocity) case is the collision energy sufficient to catastrophically disrupt 2000km objects. In the even of a disruption, the lifetime of the collision products will be very long because the largest remnant is about 1000km in size. In the more realistic case where collision velocities are set by object eccentricities and inclinations, disruption of large objects at large semi-major axes is even more difficult. This difficulty, combined with the smaller amount of starlight intercepted at such distances means that single collisions only produce a minor increase over the background level of dust (Kenyon & Bromley 2005). These probability and collision arguments suggest that a single collision is an extremely unlikely explanation for the origin of the observed dust.

The polar ring model does not have these issues. The secular evolution of particles in the 99 Her system means that particles on polar orbits suffer only minor changes in inclination and node (Fig 7). These orbits are therefore stable over the stellar lifetime so the dust could be the steady state collision products of the polar planetesimal belt. Initial misalignment is therefore the only special requirement for the polar ring model. The excellent agreement between the PACS data and a simple model generated by particles on these orbits argues strongly in favour of this interpretation.

The question is then shifted to one of the origin of the misalignment. Most binaries are thought to form through fragmentation and subsequent accretion during collapse of a molecular cloud (for a recent review see Goodwin et al. 2007). The result-

ing binary systems should be aligned with their protoplanetary disks when the separations are of order tens of AU (Bate et al. 2000). Given the 16AU separation of the 99 Her system, it therefore seems that interactions during the subsequent phase of dynamical cluster evolution are a more likely cause of a misaligned disk.

There are several ways that such a configuration could arise from interactions in a young stellar cluster. A close encounter in which a binary captures some material from the outer regions of a circumstellar disk hosted by another star seems possible. This “disk exchange” scenario requires an encounter where the binary pericenter is perpendicular to the circumstellar disk plane, and that the encounter distance and geometry captures material into orbits similar to those observed for the debris disk (e.g. most likely a prograde rather than retrograde encounter).

An alternative scenario is a stellar exchange reaction, where a binary encounters a single star that harbours a circumstellar disk. During the exchange one of the binary components is captured by the originally single star, and the other leaves (e.g. Moeckel & Goddi 2011). The post-encounter configuration is then a binary surrounded by a circumbinary disk. If the binary pericenter direction were perpendicular to the disk plane it could represent a young analogue of the 99 Her system. Such an encounter would require that the disk is not irreparably damaged by large stellar excursions during the exchange (Moeckel & Goddi 2011), but may also present a way to clear inner disk regions, thus providing a possible reason that the 99 Her disk resides at 120AU and not closer, where it could still be stable (see § 5.1.1).

Both scenarios require some degree of tuning; the encounters must happen with specific geometries to produce the observed relative binary and disk orientations. However, differences in the surface brightness between the different models in Figure 8 mean there could be some selection bias towards more disk-like structures. The advantage of the disk exchange scenario is that the cross section for interaction at a distance of about 100AU is much higher than for stellar exchange, which would need to have an encounter distance similar to the binary semi-major axis. With a factor of about ten difference in the encounter impact parameter for each scenario, the close encounter is therefore about 100 times more likely than the exchange (ignoring other constraints on geometry, configuration etc.).

In the absence of detailed simulations of encounter outcomes, some data exist to help distinguish between these two scenarios. The minimum inclination of the stellar pole for the 99 Her primary relative to the binary orbital plane is $20 \pm 10^\circ$ (Hale 1994). The inclination difference is therefore different from the binary plane with 95% confidence, and is a hint that the system may be the result of an exchange. However, the scatter in inclination differences for binaries with separations similar to that of 99 Her is about 20° (Hale 1994), which may indicate that systems with this separation are in fact aligned and the uncertainties were underestimated, or that this scatter is the intrinsic level of misalignment at these separations.

Though 99 Herculis is the first clear case of misalignment between binary and disk planes, the GG Tauri system may show a similar signature. The GG Tau system consists of an Aa/Ab binary surrounded by a circumbinary ring (Guilloteau et al. 1999; Piétu et al. 2011), and a more distant Ba/Bb pair that may be bound (Beust & Dutrey 2006). It is not clear if the inner binary is misaligned with the circumbinary disk, but is suggested because if they are aligned the ring’s inner edge is too distant

⁶ Had we found that an eccentric ring could explain the data, the same argument applied to ring spreading by pericenter precession would apply, with the same 1:10 result. The particles’ pericenter directions are unlikely to be maintained through forcing by a third (circumbinary) body as for a standard pericenter glow model, because the perturbing body would be subject to the same pericenter precession.

to be set by the binary (Beust & Dutrey 2005, 2006; Köhler 2011). However, there could also be problems if they are misaligned, because the expected disk scale height due to perturbations from the binary may be inconsistent with observations (Beust & Dutrey 2006). Though uncertain, the possible misalignment between the binary and ring planes shows that GG Tau could be a young analogue of 99 Her-like systems.

7 SUMMARY

We have modelled the resolved circumbinary debris disk in the 99 Her system. This disk is unusual because it appears misaligned with the binary plane. It can be explained as either an inclined transient ring due to a recent collision, or more likely a ring of polar orbits. The transient ring is shown to be implausible from collisional arguments. While the inclined ring cannot exist on long (secular) timescales, the polar ring can.

There appear to be two possible formation scenarios for the polar ring model, which both invoke stellar encounters. The binary may have captured material from another stars' circumstellar disk, or a new binary may have formed in a stellar exchange where one of the systems already contained a circumstellar disk.

While many binary and multiple systems are known to have debris disks, none are resolved and have orbits characterised as well as 99 Herculis. Future efforts should characterise this system further to test our interpretation and attempt to find more examples. A sample of resolved circumbinary disks would test whether disk-binary misalignment is a common outcome of star formation and cluster evolution, with implications for planetary systems around both single and binary stars.

ACKNOWLEDGMENTS

We are grateful to the referee for a thorough reading of the manuscript, especially for noting that previous 99 Her visual orbits have the wrong ascending node. This research has made use of the Washington Double Star Catalog maintained at the U.S. Naval Observatory, and the SwiftVis n -body visualisation software developed by Mark Lewis. We also thank Herve Beust for use of the HJS code, and Paul Harvey for comments on a draft of this article.

REFERENCES

- Abt, H. A. & Willmarth, D. 2006, *ApJS*, 162, 207 [ADS]
 Adelman, S. J., Caliskan, H., Kocer, D., Cay, I. H., & Gokmen Tektunali, H. 2000, *MNRAS*, 316, 514 [ADS]
 Amblard, A. et al. 2010, *A&A*, 518, L9 [ADS]
 Augereau, J. C., Nelson, R. P., Lagrange, A. M., Papaloizou, J. C. B., & Mouillet, D. 2001, *A&A*, 370, 447 [ADS]
 Bate, M. R., Bonnell, I. A., Clarke, C. J., Lubow, S. H., Ogilvie, G. I., Pringle, J. E., & Tout, C. A. 2000, *MNRAS*, 317, 773 [ADS]
 Beust, H. 2003, *A&A*, 400, 1129 [ADS]
 Beust, H. & Dutrey, A. 2005, *A&A*, 439, 585 [ADS]
 —. 2006, *A&A*, 446, 137 [ADS]
 Boesgaard, A. M., McGrath, E. J., Lambert, D. L., & Cunha, K. 2004, *ApJ*, 606, 306 [ADS]
 Churcher, L. J., Wyatt, M. C., Duchêne, G., Sibthorpe, B., Kennedy, G., Matthews, B. C., Kalas, P., Greaves, J., Su, K., & Rieke, G. 2011, *MNRAS*, 417, 1715 [ADS]
 Dommangen, J. & Nys, O. 2002, *VizieR Online Data Catalog*, 1274, 0 [ADS]
 Doolin, S. & Blundell, K. M. 2011, *ArXiv e-prints*, (1108.4144) [ADS]
 Farago, F. & Laskar, J. 2010, *MNRAS*, 401, 1189 [ADS]
 Fruchter, A. S. & Hook, R. N. 2002, *PASP*, 114, 144 [ADS]
 Goodwin, S. P., Kroupa, P., Goodman, A., & Burkert, A. 2007, *Protostars and Planets V*, 133 [ADS]
 Gratton, R. G., Carretta, E., & Castelli, F. 1996, *VizieR Online Data Catalog*, 331, 40191 [ADS]
 Griffin, M. J. et al. 2010, *A&A*, 518, L3 [ADS]
 Guilloteau, S., Dutrey, A., & Simon, M. 1999, *A&A*, 348, 570 [ADS]
 Hale, A. 1994, *AJ*, 107, 306 [ADS]
 Hartkopf, W. I., Mason, B. D., & Worley, C. E. 2001, *AJ*, 122, 3472 [ADS]
 Hauck, B. & Mermilliod, M. 1997, *VizieR Online Data Catalog*, 2215, 0 [ADS]
 Henry, T. J. & McCarthy, Jr., D. W. 1993, *AJ*, 106, 773 [ADS]
 Ishihara, D. et al. 2010, *A&A*, 514, A1 [ADS]
 Kenyon, S. J. & Bromley, B. C. 2005, *AJ*, 130, 269 [ADS]
 Koerner, D. W., Kim, S., Trilling, D. E., Larson, H., Cotera, A., Stapelfeldt, K. R., Wahhaj, Z., Fajardo-Acosta, S., Padgett, D., & Backman, D. 2010, *ApJ*, 710, L26 [ADS]
 Köhler, R. 2011, *A&A*, 530, A126 [ADS]
 Kozai, Y. 1962, *AJ*, 67, 591 [ADS]
 Li, A. & Greenberg, J. M. 1997, *A&A*, 323, 566 [ADS]
 Lidov, M. L. 1962, *Planet. Space Sci.*, 9, 719 [ADS]
 Mason, B. D., Wycoff, G. L., Hartkopf, W. I., Douglass, G. G., & Worley, C. E. 2011, *VizieR Online Data Catalog*, 1, 2026 [ADS]
 Matthews, B. C. et al. 2010, *A&A*, 518, L135 [ADS]
 Mermilliod, J. C. 2006, *VizieR Online Data Catalog*, 2168, 0 [ADS]
 Moeckel, N. & Goddi, C. 2011, *ArXiv e-prints*, (1109.2007) [ADS]
 Moshir, M. & et al. 1990, in *IRAS Faint Source Catalogue*, version 2.0 (1990), 0 [ADS]
 Nordström, B., Mayor, M., Andersen, J., Holmberg, J., Pont, F., Jørgensen, B. R., Olsen, E. H., Udry, S., & Mowlavi, N. 2004, *A&A*, 418, 989 [ADS]
 O'Brien, D. P. & Greenberg, R. 2003, *Icarus*, 164, 334 [ADS]
 Ott, S. 2010, in *Astronomical Society of the Pacific Conference Series*, Vol. 434, *Astronomical Data Analysis Software and Systems XIX*, ed. Y. Mizumoto, K.-I. Morita, & M. Ohishi, 139 [ADS]
 Perryman, M. A. C. & ESA, eds. 1997, *ESA Special Publication*, Vol. 1200, *The HIPPARCOS and TYCHO catalogues. Astrometric and photometric star catalogues derived from the ESA HIPPARCOS Space Astrometry Mission* [ADS]
 Phillips, N. M., Greaves, J. S., Dent, W. R. F., Matthews, B. C., Holland, W. S., Wyatt, M. C., & Sibthorpe, B. 2010, *MNRAS*, 403, 1089 [ADS]
 Piétu, V., Gueth, F., Hily-Blant, P., Schuster, K.-F., & Pety, J. 2011, *A&A*, 528, A81 [ADS]
 Pilbratt, G. L., Riedinger, J. R., Passvogel, T., Crone, G., Doyle, D., Gageur, U., Heras, A. M., Jewell, C., Metcalfe, L., Ott, S., & Schmidt, M. 2010, *A&A*, 518, L1 [ADS]
 Poglitsch, A. et al. 2010, *A&A*, 518, L2 [ADS]

- Rieke, G. H. et al. 2004, *ApJS*, 154, 25 [ADS]
— 2008, *AJ*, 135, 2245 [ADS]
- Scardia, M., Prieur, J.-L., Pansecchi, L., Argyle, R. W., & Sala, M. 2010, *Astronomische Nachrichten*, 331, 286 [ADS]
- Scardia, M., Prieur, J.-L., Pansecchi, L., Argyle, R. W., Sala, M., Basso, S., Ghigo, M., Koechlin, L., & Aristidi, E. 2008, *Astronomische Nachrichten*, 329, 54 [ADS]
- Söderhjelm, S. 1999, *A&A*, 341, 121 [ADS]
- Stewart, S. T. & Leinhardt, Z. M. 2009, *ApJ*, 691, L133 [ADS]
- Takeda, Y. 2007, *PASJ*, 59, 335 [ADS]
- Trilling, D. E., Stansberry, J. A., Stapelfeldt, K. R., Rieke, G. H., Su, K. Y. L., Gray, R. O., Corbally, C. J., Bryden, G., Chen, C. H., Boden, A., & Beichman, C. A. 2007, *ApJ*, 658, 1289 [ADS]
- van Leeuwen, F., ed. 2007, *Astrophysics and Space Science Library*, Vol. 350, *Hipparcos, the New Reduction of the Raw Data* [ADS]
- van Leeuwen, F. 2008, *VizieR Online Data Catalog*, 1311, 0 [ADS]
- Verrier, P. E. & Evans, N. W. 2008, *MNRAS*, 390, 1377 [ADS]
— 2009, *MNRAS*, 394, 1721 [ADS]
- Wiegert, P. A. & Holman, M. J. 1997, *AJ*, 113, 1445 [ADS]
- Wyatt, M. C. & Dent, W. R. F. 2002, *MNRAS*, 334, 589 [ADS]
- Wyatt, M. C., Dermott, S. F., Telesco, C. M., Fisher, R. S., Grogan, K., Holmes, E. K., & Piña, R. K. 1999, *ApJ*, 527, 918 [ADS]
- Wyatt, M. C., Smith, R., Greaves, J. S., Beichman, C. A., Bryden, G., & Lisse, C. M. 2007a, *ApJ*, 658, 569 [ADS]
- Wyatt, M. C., Smith, R., Su, K. Y. L., Rieke, G. H., Greaves, J. S., Beichman, C. A., & Bryden, G. 2007b, *ApJ*, 663, 365 [ADS]